PRACTICAL ELECTRON MICROSCOPY IN MATERIALS SCIENCE

Monograph Four

# 4 Typical Electron Microscope Investigations

J W Edington

*Philips Technical Library*

*Monographs in Practical Electron Microscopy in Materials Science*

# 4

# TYPICAL ELECTRON MICROSCOPE INVESTIGATIONS

J. W. EDINGTON

*Department of Metallurgy and Materials Science, University of Cambridge, Cambridge, England*

SBN 333 18640 0

First published 1976 by
THE MACMILLAN PRESS LTD
London and Basingstoke
Associated companies in New York Dublin
Melbourne Johannesburg and Madras


**PHILIPS**



Printed in Great Britain by
Thomson Litho Ltd, East Kilbride, Scotland

# PREFACE

This is the fourth of a series of monographs on electron microscopy aimed at users of the equipment. They are written as both texts and sources of reference emphasising the applications of electron microscopy to the characterisation of materials.

In some places the author has referred the reader to material appearing in other monographs of the series:

1. *The Operation and Calibration of the Electron Microscope.*
2. *Electron Diffraction in the Electron Microscope.*
3. *Interpretation of Transmission Electron Micrographs.*

**Abbreviations and Symbols Frequently Used in this Monograph**

| | |
|---|---|
| BF | bright field (image) |
| DF | dark field (image) |
| CDF | centred dark field (image) |
| WB | weak beam (image) |
| DP | diffraction pattern |
| SADP | selected area diffraction pattern |
| SRO | short-range order |
| APB | antiphase domain boundary |
| $\boldsymbol{g}$ | a vector normal to the reflecting plane |
| $\boldsymbol{s}$ | the deviation from the Bragg reflection position |
| $\xi_g$ | the extinction distance |
| $w$ | $s\xi_g$ |
| $\boldsymbol{b}$ | the Burgers vector of an undissociated dislocation |
| $\boldsymbol{b}_p$ | the Burgers vector of a partial dislocation |
| $\boldsymbol{u}$ | the line vector of a dislocation |
| FN | the upward drawn foil normal (normal to the specimen surface) |
| $\boldsymbol{B}$ | the upward drawn incident beam direction in the specimen, that is opposite to the direction of the electron beam |
| ANO | anomalous absorption coefficient |

# CONTENTS

## 4 TYPICAL ELECTRON MICROSCOPE INVESTIGATIONS

# 4. TYPICAL ELECTRON MICROSCOPE INVESTIGATIONS

## I. APPROACH TO PROBLEMS

Microstructural studies of metals and materials using transmission electron microscopy frequently involve the correlation of information present in both images and diffraction patterns. This process may be relatively easy if the interpretation of the images and diffraction patterns is simple. However, in many cases the interpretation of both images and diffraction patterns is difficult because a whole range of different finely dispersed crystal defects may be present simultaneously. Such problems frequently arise in complex commercial alloys when detailed quantitative interpretation of the microstructure can be extremely difficult. The following problems are typical.

(1) Separation and identification of different crystal defects that produce superficially similar images or diffraction effects.

(2) Identification and detailed analysis of different crystal defects responsible for a specific effect such as streaking in diffraction patterns.

(3) Collection of the maximum amount of quantitative information about all, or particular aspects of, the defect population of the crystal.

It is the purpose of the first part of this section to indicate general rules for obtaining detailed quantitative information from both simple and complex microstructures in a wide range of materials. Part II summarises some of the information in sections 2 and 3 to enable identification of crystal defects responsible for superficially similar features of microstructures and diffraction patterns. Finally parts III and IV contain a number of specific examples of detailed microstructural studies of a wide range of simple and complex materials.

### 4.1 General Rules for the Investigation of Microstructures

It is important to note that a series of detailed rules for investigation of complex microstructures cannot be formulated because of the diverse nature of the problems likely to be encountered. Each problem must be treated on its merits. However, a general approach would include extensive use of the following.

(1) CDF images (defined in section 1.5.2) using all of those features of the diffraction pattern, such as extra spots or streaks, to identify the features of the microstructure from which they arise, see sections 2.16–2.19.

(2) Detailed comparison of CDF and BF images which is the basis for the identification of specific crystal defects producing superficially similar (for example, fringe) images.

(3) Specimen tilting to determine the three-dimensional details of additional features of the SADP at or near a range of low-index $\boldsymbol{B}$, see section 2.10.1.3. This approach enables the type of crystal defect responsible for the fine structure of the SADP to be determined. Alternatively, by making use of CDF using precipitate reflections, particle shapes, densities, etc., may be obtained.

(4) Specimen tilting in a known sense using Kikuchi maps where detailed analysis of the sense of dislocation loops, $\boldsymbol{b}$ of dislocations, etc., is required, see section 2.10.1.1.

(5) Small amounts of specimen tilt to change the value of $\pm s$, $\pm g$ for two-beam conditions to determine the conditions for maximum visibility of a particular crystal defect, see sections 2.10.1, 2.10.2.

(6) Weak beam images to improve resolution when a high density of defects is present, see section 3.17.

(7) Imaging under a series of well-defined two-beam conditions, that is only one strong diffracted beam present in the diffraction pattern, see section 3.2.

## Ii. DIFFERENTIATION BETWEEN SIMILAR TYPES OF IMAGE

The characteristic images of the defects discussed in section 3 may be used to identify crystal defects observed in thin foils. Clearly a large number of crystal defects such as incoherent large precipitates, dislocations, etc., may be readily identified on the basis of their overall morphology. However, there

are three classes of image for which this is not true.

(1) Planar defects giving rise to fringe images.
(2) Small clusters giving rise to strain contrast images.
(3) Small clusters giving rise to structure factor contrast.

Within these classes different crystal defects can be responsible for the general form of the image but their detailed image characteristics described in section 3 may be used to identify the defect responsible for the image and in some cases to specify it completely crystallographically, for example extrinsic/intrinsic nature of a stacking fault.

In practice, the following information may be required to identify a particular defect.

(1) Behaviour in BF and CDF (with opposite $\boldsymbol{g}$) at $s = 0$.
(2) Behaviour in BF for $\pm\boldsymbol{g}$.
(3) Behaviour in BF for different $\boldsymbol{g}$.
(4) Behaviour for through-focus series, that is underfocus–focus–overfocus sequences.

It is most important to realise that it is sometimes not possible to identify a crystal defect purely on the basis of its contrast behaviour. This is particularly important for small clusters, for example voids, precipitates, gas bubbles, dislocation loops. In these cases metallurgical information such as the behaviour of the defect on annealing is frequently essential to be certain of an identification.

## 4.2 Characterisation of Planar Defects

Planar defects produce fringe images if they lie on an inclined plane running from the top to the bottom of the foil as shown schematically in figure 3.29(a). The major characteristics of such images, based on sections 3.6, 3.7, 3.8, are summarised in table 4.1 and are enough to enable

Table 4.1 Important image characteristics for different types of planar crystal defect

| Defect | Type of fringe | Spacing | Visibility | Characteristics | Quantitative information | Reference |
|---|---|---|---|---|---|---|
| *stacking fault* forms $\alpha$ fringe $\alpha \neq n\pi$ | *displacement*, fringes parallel to intersection of defect plane with the foil surface $\alpha = 2\pi\boldsymbol{g}\cdot\boldsymbol{R}_F : \boldsymbol{R}_F$ is displacement vector $\alpha = \pm\frac{2\pi}{3}, \frac{4\pi}{3}$ or 0 for stacking fault | $\frac{1}{2}\xi_g$ at $s = 0$ $\xi_g/(1+w^2)^{1/2}$ at $s \neq 0$ | best at $s = 0$ for both BF and DF | BF image symmetric, that is fringes at top and bottom of foil either both bright or dark. DF image asymmetric, that is opposite contrast fringes at top and bottom of foil | fringes invisible $\boldsymbol{g}\cdot\boldsymbol{R}_F = 0$. Use to determine direction of $\boldsymbol{R}_F$. Intrinsic/extrinsic nature determined by a number of techniques for $s = 0$ only. Simplest is use dark field image, transfer $\boldsymbol{g}$ to positive print, origin of $\boldsymbol{g}$ set at centre of fringes. If $\boldsymbol{g}$ points towards bright outer fringe fault is extrinsic. If dark fringe fault is intrinsic for class $B$ {111} {220} {400} reflections. For class A {200} {222} {440} reflections reverse is true | section 3.6.1 |
| *planar precipitate* with small misfit forms $\alpha$ fringe $\alpha \neq n\pi$ | *displacement*, fringes parallel to the intersection of the habit plane with the foil surface $\alpha = 2\pi\boldsymbol{g}\cdot\boldsymbol{R}_n = 0$ or fraction; $\boldsymbol{R}_n$ is displacement vector normal to habit plane | $\frac{1}{2}\xi_g$ at $s = 0$ | best at $s = 0$ in BF and DF | BF image symmetric, DF image asymmetric | fringes invisible $\boldsymbol{g}\cdot\boldsymbol{R}_n = 0$. Use to determine direction of $\boldsymbol{R}_n$. Precipitate smaller or larger than the matrix lattice may be determined using rules above for stacking fault. N.B. only valid if precipitate very thin and not diffracting | section 3.6.3 |
| *antiphase domain boundaries* form $\alpha = \pi$ fringes | *displacement*, fringes parallel to the intersection of the habit plane with the foil surface $\alpha = 2\pi\boldsymbol{g}\cdot\boldsymbol{P}$, where $\boldsymbol{P}$ is displacement vector of APB. $\alpha = 0$ or $\pi$ | $\frac{1}{2}\xi_g$, $s = 0$ | best at $s = 0$ in BF and DF | BF image symmetric, DF image symmetric and exactly opposite of BF | fringes invisible $\boldsymbol{g}\cdot\boldsymbol{P} = 0$ (can be used to determine direction of $\boldsymbol{P}$) | section 3.7 |

Table 4.1 (*continued*)

| Defect | Type of fringe | Spacing | Visibility | Characteristics | Quantitative information | Reference |
|---|---|---|---|---|---|---|
| *δ boundary*, for example between two ordered domains 1,2 with slightly different lattice parameters | δ, fringes run parallel to the intersection of the habit plane with the foil surface | $\sim\xi_g$ but depends sensitively on $s$ | best for $s_1 = -s_2$, that is same value in both domains | BF image asymmetric, DF image symmetric (reverse of stacking fault behaviour) | fringes invisible when $\Delta\boldsymbol{g} = \boldsymbol{g}_1 - \boldsymbol{g}_2 = 0$, that is no difference in $\boldsymbol{g}$ across boundary. May be used to determine the direction of distortion | section 3.8 |
| *α–δ boundaries*, for example thick precipitates | α–δ, fringes parallel to intersection of habit plane with the foil surface | depends on relative α–δ contributions | best at $s > 0$ but small | faint fringes—intermediate between α and δ boundaries | may be identified but difficult | section 3.9 |
| *thickness fringes* | fringes following regions of uniform thickness, that is depth contours at edge of foil or grain boundary fringes when only one grain diffracting | $\xi_g$ at $s = 0$ $\xi_g/(1+w^2)^{1/2}$ at $s \neq 0$ | best at $s = 0$ | fringes reverse contrast in BF and DF and join grain boundary fringes | used to determine foil thickness $= (n+\frac{1}{2})\xi_g$ black fringes, BF, at $s = 0$, where $n$ = number of fringes | section 3.2.3.1 |
| *structure factor fringe* at precipitates, voids, etc. | fringes parallel to the intersection of the habit plane to the foil surface. N.B. Cavity $\alpha = 2\pi s t_c$ ($t_c$ = cavity thickness) | | best at $s \neq 0$ | invisible $s = 0$. Weak for thick specimens when absorption important | invisible $s = 0$, visible $s \neq 0$ may be used for identification when absorption unimportant | section 3.12 |
| Moiré fringes at interfaces | fringes perpendicular to the operative $\Delta\boldsymbol{g} = \boldsymbol{g}_1 - \boldsymbol{g}_2$ | $\lvert\boldsymbol{g}_1 - \boldsymbol{g}_2\rvert^{-1}$ | $s$ small and positive with strong intensity in diffracted beam in each crystal | direction and spacing changes with operative reflection | Moiré fringes may be recognised by changing the operative reflection when the direction of the fringes will change | section 3.21 |

identification. In effect all that is required is comparison of either BF and CDF images or CDF images and SADP.

### 4.2.1 *Identification of the Defect Responsible for Fringe Images*

Previous sections include examples of the identification of stacking faults (section 3.6) planar precipitates exhibiting α fringes (section 3.11.3) antiphase ($\pi$) domain boundaries (section 3.7) and δ boundaries (section 3.8) using the criteria in table 4.1 combined with some of those described in the relevant sections in section 3. In this section we describe one method of determining the sense of a stacking fault and the identification of a mixed α–δ boundary.

#### 4.2.1.1 *Stacking fault (after M. N. Thompson)*

Figure 4.1 shows a stacking fault which is identified, in this case, by using only a BF image and a SADP (van Landuyt *et al.*, 1966b). The method relies on the 'effective' streaking of the reciprocal lattice points perpendicular to the fault habit plane which produces satellite spots as described in section 2.17.1. The operative reflection in figure 4.1 was $(\bar{2}\bar{2}2)$ with $s < 0$ delineated by the position of the bright Kikuchi line inside this spot (see section 2.10.2). The inset diffraction spot is the $(22\bar{2})$ opposite reflection for which, because of the curvature of the Ewald sphere $s > 0$. The perpendicular direction of the lines joining the satellite spots c and d to the higher intensity matrix spot m indicates that they originate from the stacking faults of the type c and d respectively inclined on different {111} planes, that is mc and md are perpendicular to the line of intersection of the fault planes and the foil surface—approximately perpendicular to the fringes. The location of the diffraction spots d and c to the right of m and the

$s > 0$ excitation error indicates that the slopes of the faults c and d are as depicted in figure 4.1(c). In the micrograph the top and bottom of the faults are represented by T and B.

In relation to the single fault c the following information has been established.

(1) $\boldsymbol{g}$ is $[\bar{2}\bar{2}2]$ class A, table 4.2.

(2) The relative orientation of the fault and $\boldsymbol{g}$ is as shown in figure 4.1(c).

(3) The extreme dark fringes in the positive BF print, figure 4.1(a), are dark–dark.

Table 4.2

| Diffraction vector | Class |
|---|---|
| [200] | A |
| [222] | A |
| [440] | A |
| [400] | B |
| [111] | B |
| [220] | B |

Reference to tables 4.2 and 4.3, taken from van Landuyt *et al.* (1966b), establish fault c as intrinsic. Analysis of the other stacking faults is prevented by the overlapping effects which are responsible for the fringe shifts, etc., see section 3.6.1.2.

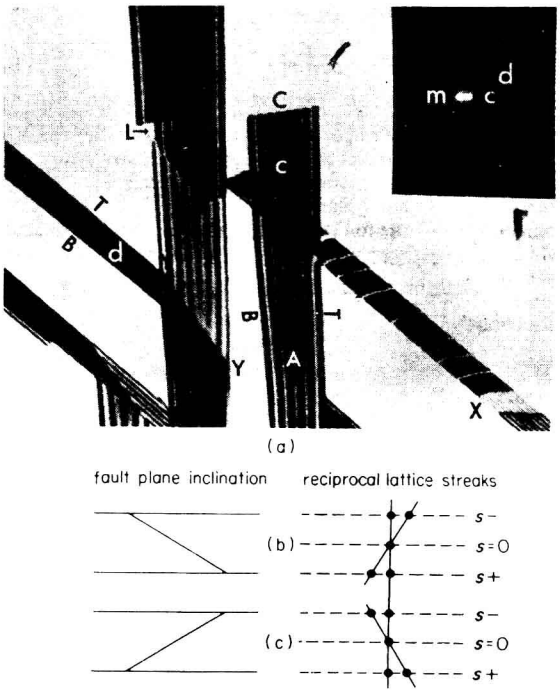


Figure 4.1 (a) The relationship between the fine structure of the diffraction spot and the BF image of intersecting stacking faults. Inset $(22\bar{2})$ diffraction spot $s$ positive. (b), (c) The relationship between fault plane inclination, reciprocal lattice streaking, and the dependence of matrix and satellite separation on the deviation parameter $s$. The dashed line represents the Ewald sphere

Table 4.3

| | Bright field | | | | Dark field | | | |
|---|---|---|---|---|---|---|---|---|
| $\boldsymbol{g}$ → | A | | B | | A | | B | |
| Extrinsic | D | D | B | B | B | D | D | B |
| | B | B | D | D | B | D | D | B |
| $\boldsymbol{g}$ → | Bright field | | | | Dark field | | | |
| | A | | B | | A | | B | |
| Intrinsic | B | B | D | D | D | B | B | D |
| | D | D | B | B | D | B | B | D |

——— fringe corresponding to top surface; — — — fringe corresponding to bottom surface. B and D mean bright and dark, respectively, that is the nature of the extreme fringes.
From van Landuyt *et al.* (1966b).

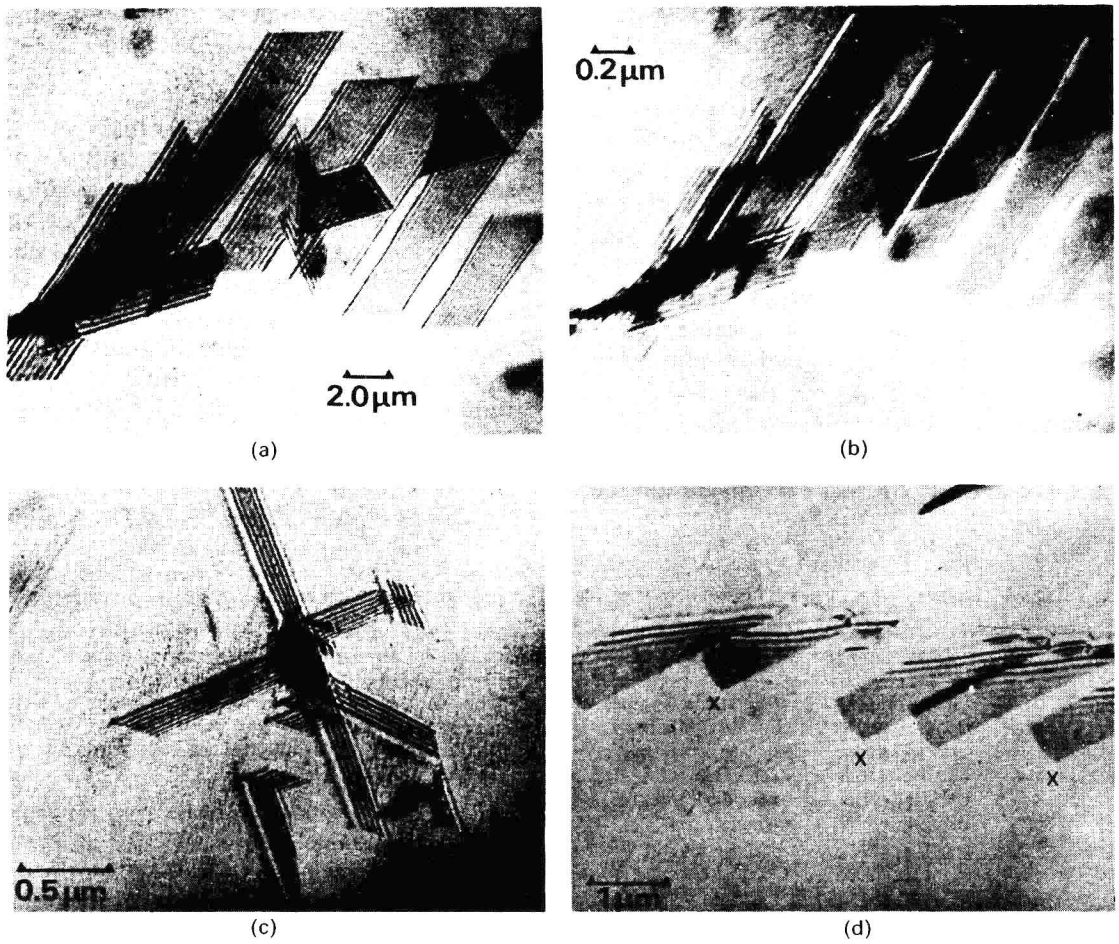


Figure 4.2 Images of plate-shaped precipitates in niobium: (a) BF; (b) CDF; (c) intersection of fringe patterns; (d) fringe systems ending inside the foil at X where features are observed in disagreement with the stacking fault hypothesis [From van Landuyt *et al.* (1966a), courtesy of *Physica Status Solidi*]

4.2.1.2 *Mixed $\alpha$–$\delta$ fringes (after J. van Landuyt)*

Figure 4.2 shows the identification of mixed $\alpha$–$\delta$ fringes due to van Landuyt *et al.* (1966a). Close examination of the fringes in BF and CDF reveals that their central parts are different from the outer parts, see figure 4.2(a), (c). This may be interpreted in terms of a central region of overlap of two closely spaced interfaces whereas the outer parts on both sides are associated with single interfaces, that is the geometry in figure 3.37(a). Further observations are as follows.

(1) There is no difference in background on either side of the fringe patterns.

(2) The BF image is symmetrical but the DF is asymmetrical in region AA but symmetrical in region BB, figure 4.2(b).

(3) Partial dislocations were not necessarily present along the border of the fringe patterns, figure 4.2(d).

The interpretation is as follows.

(1) The fringes are caused by thin precipitate plates, that is region II, figure 3.37(a), would be a precipitate. This is consistent with observations that these defects protrude from the foil edge.

(2) The fringes are due to overlapping $\alpha$–$\delta$ interfaces. The $\delta$ component could be due to a slight misorientation of the reflecting planes in both phases, together with possible differences in $\xi_g$ and absorption length. The $\alpha$ component may arise from the different phase angles produced in the different crystals.

The defects are not displacement fringes because, if the contrast were due to a shift between the crystal parts on either side of the precipitate, the region of overlap would exhibit the $\alpha$ fringes described in section 3.6.1, whereas the non-overlap parts would exhibit wedge fringes. Although region AA has $\alpha$ fringes BB does not, that is BF and DF images are the same.

The interfaces are not $\delta$ fringes because, if they were, they should have equal and opposite components as the background intensity is the same on either side. Closely overlapping $\delta$ interfaces produce an $\alpha$ fringe pattern in the overlapping part

but the outer fringes of the images in BF would be opposite in sign, see section 3.8.1.2, which they are not.

The interfaces are not $\alpha$ interfaces because (1) the overlapping region should have $\alpha$ fringes as observed, but (2) the outer fringes should have opposite contrast in either BF if the signs of $\alpha$ are opposite or DF if $\alpha_1$ and $\alpha_2$ are both positive. This is not observed.

The interfaces do not arise from a shift in the two parts of crystal 1, figure 3.37(a), because, if the precipitate does not diffract, the region of overlap would exhibit $\alpha$ fringes whereas the non-overlap parts would exhibit wedge fringes, see van Landuyt *et al.* (1965). Although region AA exhibits $\alpha$ fringes BB does not and the BF and DF images are the same.

## 4.3 Characterisation of the Strain Field Images of Precipitates, Loops, Gas Bubbles, End-on Dislocations and Etch Pits

These defects produce either small black/white lobe contrast or large black/black lobes with occasional examples of large black/white lobes, see section 3.11.1.2. The characteristics of these images are discussed below and summarised in tables 4.4 and 4.5. It is important to realise that complete identification based on their contrast behaviour in BF and CDF images can be difficult. Additional metallurgical information is frequently required, for example the behaviour of the defect on annealing.

### 4.3.1 *Small Black-dot or Black/White Lobe Images*

The size of these images is usually $\ll \xi_g$ and they

Table 4.4 Image characteristics of crystal defects giving dot or small lobe (black/white) images $\lesssim 0.25\xi_g$ in diameter

| Defect | Type of image | Visibility, BF | Characteristics, BF | Quantitative information | Reference |
|---|---|---|---|---|---|
| *Frank loop* $< 100$ Å *diameter*, for example $\boldsymbol{b} = \frac{1}{3}\langle 111\rangle$ f.c.c. | lobes of black/white contrast near top and bottom of foil. At critical depths black-dot contrast | best at small values $s > 0$ slightly dark background, that is thickness $= (n \pm \frac{1}{4})\xi_g$, near dark thickness fringes | black/white contrast reverses depending on depth, that is at $0.3\xi_g$ $0.75\xi_g$ and does not occur below $1.25\xi_g$. Black dots at $0.3\xi_g$ and $0.75\xi_g$ and within centre of foil independent of $\pm\boldsymbol{g}$. The line $\boldsymbol{l}$ joining centre of black and white lobes is parallel to projection of $\boldsymbol{b}$ | with *considerable* care the sense and Burgers vector of loops may be determined | section 3.5.5 |
| *small loops with a shear component* | images complex and interpretation is not covered by theory at present | | | | |
| *small precipitates* $\boldsymbol{g}\varepsilon r_0^3/\xi_g^2 < 0.2$ (a) spherically symmetric strain fields | small black/white lobes | as for Frank loops | black/white contrast changes with depth as for Frank loops (see above) and the line $\boldsymbol{l}$ joining centre of the black and white lobes is parallel to $\boldsymbol{g}$ | with *considerable* care the sense of the strain field may be determined | section 3.11.1 |
| (b) asymmetric strain fields, that is non-spherical particle and/or elastically anisotropic matrix | as for (a) | as for (a) | as for (a) but $\boldsymbol{l}$ not always parallel to $\boldsymbol{g}$ | with *considerable* care it should be possible to determine the sense of strain field using the rules for (a). However, no theoretical background | section 3.11.1 |
| *gas bubbles* with spherically symmetric or asymmetric strain fields | as for (a) | as for (a) | images have same form as (a), (b) above. In the case of bubbles $d \lesssim 0.3\xi_g$ these may only be visible under dynamical contrast conditions. However, show characteristic through-focus properties, that is overfocus properties dark spot, underfocus bright spot | with considerable care it should be possible to determine the sense of the strain field as for (a), (b) above | section 3.13 |

can arise from precipitates, gas bubbles, dislocation loops or etch pits with a strain field, see table 4.4. The image characteristics of etch pits with strain field have not been studied and cannot be included in table 4.4. Consequently, the best method of detecting such a defect would be stereo microscopy which should demonstrate that the defects lie at the surface. The important image characteristics of the remaining defects are listed in table 4.4 and they may be supplemented by details from sections 3.5.5, 3.11.1 and 3.13.

It is important to realise that, from an experimental and theoretical viewpoint, the contrast behaviour of the following defects is reasonably well understood: Frank loops for isotropic elasticity; precipitates and gas bubbles with spherically symmetrical strain fields. For the other defects complete information is not yet available.

The following information may be readily obtained.

(1) Frank loops may be distinguished from precipitates/bubbles with spherically symmetrical strain fields because $\boldsymbol{l}$ is always approximately parallel to the projection of $\boldsymbol{b}$ with different $\boldsymbol{g}$ whereas $\boldsymbol{l}$ is parallel to $\boldsymbol{g}$ in the latter case.

(2) The sense of the displacement associated with Frank loops, precipitates and bubbles with spherically symmetrical strain fields may be determined using the approach outlined in section 3.5.6.2.

The following experiments are extremely difficult.

(1) To distinguish between gas bubbles and small precipitates with spherically symmetrical strain fields. In this case the specimen may be tilted to kinematical conditions and a through-focus series obtained which may enable the bubbles to be identified. Alternatively, extra spots may be present in the SADP from precipitates if the volume fraction is large.

(2) To distinguish between precipitates with edge loop type asymmetric strain fields, for example precipitate plates and Frank loops.

(3) Any problems associated with small plate defects (loops, precipitates) with a shear component of the strain field.

#### 4.3.1.1 *Small precipitates versus Frank loops (after R. B. Scarlin)*

A very good example of this is shown below describing the differentiation between Frank loops and fine misfitting 'matrix dot' TiC precipitates in a nickel-base alloy. In a number of materials, MC carbides such as TiC form small, finely dispersed, cuboidal precipitates (edge length $\lesssim 100$ Å) with a cube–cube orientation relationship to the matrix. Because of the misfit strain, these defects exhibit small black/white strain field images. Figure 4.3(a) shows a region of a Ni–2 wt % Ti–0.3 wt % C alloy aged at 600 °C for 200 hours. Two types of defect are present, large black/black lobes of contrast at B and small black/white contrast lobes at A. There are no extra spots or streaks in SADP. The black/black lobes are typical of the strain field image from a precipitate with $P_s \gtrsim 0.2$, section 3.11.1.2, whereas the small black/white images could be either fine-scale precipitate or Frank loops. In fact they were shown to be $\frac{1}{3}\langle 111\rangle$ vacancy Frank loops, see section 3.5.6.1.

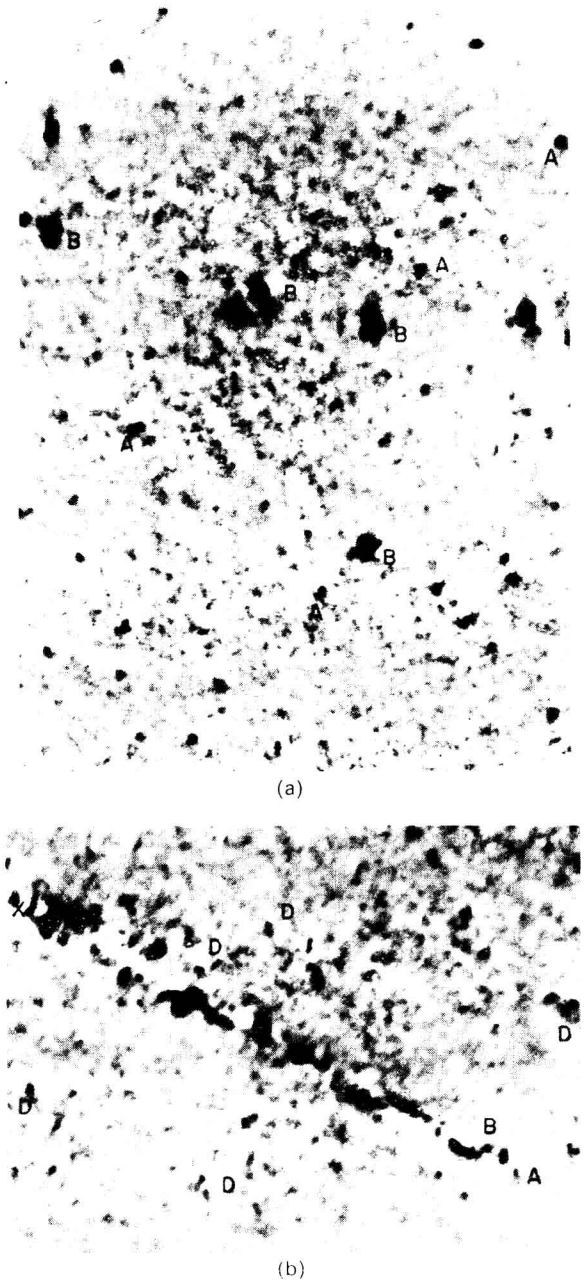


Figure 4.3 BF electron micrographs of TiC particles B. (a) In quenched and aged Ni–4.47 wt % Ti–1.96 wt % C alloy in the presence of small Frank loops A. (b) A row of very small particles intersecting the bottom surface of the specimen at A

Table 4.5 Image characteristics of crystal defects giving large ($r > 0.25\xi_g$) black/black or black/white lobe contrast

| Defect | Type of image | Visibility, BF | Characteristics, BF | Quantitative information | Reference |
|---|---|---|---|---|---|
| *precipitate* with (a) spherically symmetrical strain field, $P_s = \boldsymbol{g}\varepsilon r_0^3/\xi_g^2 \gtrsim 0.2$ | black/black lobes in foil, black/white lobes if precipitate lies within $\xi_g$ of surface | best at $s > 0$ and at thicknesses with $(n \pm \frac{1}{4})\xi_g$ which exhibit slight background contrast | image diameter $\sim \xi_g$. Large black/black lobes line of no contrast always perpendicular to $\boldsymbol{g}$. Black/white reverses on reversing $\boldsymbol{g}$ but black/black images unaffected | with care the sense of the strain field may be determined from black/white images and its value estimated from black/black images | section 3.11.2.1 |
| (b) asymmetric strain field, that is non-spherical particle or elastically anisotropic matrix, $P_s = \boldsymbol{g}\varepsilon r_0^3/\xi_g^2 \gtrsim 0.2$ | not quantified but assumed to be similar to (a) | as for (a) | the same general behaviour as (a) would be expected and has been proved for Co particles in Cu[a]. N.B. Line of no contrast not oeroendicular to $\boldsymbol{g}$ for all $\boldsymbol{g}$ and sometimes curved[b] | possible with care to determine the sense of the strain field | section 3.11.1 |
| *gas bubbles* | as for (a) | as for (a) | some general features as above (a), (b) for precipitates except that the through-focus properties are underfocus bright spot, overfocus dark spot | with considerable care the sense of the strain field can be determined and the magnitude estimated using the Ashby–Brown analysis for spherically symmetrical strain fields | section 3.13 |
| *end-on dislocations* | black/white lobes | best at $s > 0$ | image diameter $\sim \xi_g$, stronger images for screw than edge dislocations | the sense of the dislocation RH or LH screw may be determined | section 3.4.8 |
| *medium-sized perfect loops*, 100–500 Å diameter, for example $\boldsymbol{b} = \frac{1}{2}\langle 110\rangle$ f.c.c. $\frac{1}{2}\langle 111\rangle$ b.c.c. | resolvable loop | $s > 0$ but small use thicknesses $(n \pm \frac{1}{4})$ $\xi_g$ to give some background contrast | contrast is not significantly dependent on the depth of the loops in the foil. However, dot changes to double black lobe $\pm\boldsymbol{g}$ | with considerable care the sense and Burgers vector of the loop may be determined. However, consistent results may only be obtained for a fraction of the loops | sections 3.5.3, 3.5.4 |
| *large perfect edge loops*, diameter > 500 Å $\boldsymbol{b} = \frac{1}{2}\langle 110\rangle$ f.c.c. $\frac{1}{2}\langle 111\rangle$ b.c.c. | resolvable loop | best at small values of $s > 0$ | contrast not significantly dependent on the depth of the loop in the foil but loop image changes size $\pm\boldsymbol{g}$ | the Burgers vector and sense of the loop may be obtained reasonably easily | sections 3.5.1, 3.5.2 |
| *medium-sized Frank loops* $\boldsymbol{b} = \frac{1}{3}\langle 111\rangle$ f.c.c. | resolvable loop | best at small values of $s > 0$ | contrast not significantly dependent on the depth of the loop in the foil but fringes from stacking fault are not observed | the Burgers vector of loop may be obtained using $\boldsymbol{g}\cdot\boldsymbol{b} = 0$ and $\boldsymbol{g}\cdot\boldsymbol{b} = 1$ conditions but avoiding $\boldsymbol{g}\cdot\boldsymbol{b} = \frac{1}{3} \pm \frac{2}{3}$. Loop may be separated from perfect loop by reversing $\boldsymbol{g} \pm [200]$ when Frank loop reverses contrast | sections 3.5.3, 3.5.4 |
| *large Frank loops*, diameter $\gtrsim$ 500 Å $\boldsymbol{b} = \frac{1}{3}\langle 111\rangle$ f.c.c. | resolvable loop containing stacking fault fringes | best at small values of $s > 0$ | contrast of fringes better if loop near top and bottom of foil and also better for first-order reflections | the Burgers vector of loop may be obtained using $\boldsymbol{g}\cdot\boldsymbol{b} = 0$ and 1 conditions but avoiding $\boldsymbol{g}\cdot\boldsymbol{b} = \pm\frac{1}{3}, \frac{2}{3}$. Sense may be determined using $\boldsymbol{g}\cdot\boldsymbol{b} = \pm\frac{4}{3}$ | sections 3.5.1, 3.5.2 |

[a] McIntyre and Brown (1966).
[b] Degischer (1972).

These loops are concluded to arise from ion damage in the microscope for the following reasons.

(1) They lie near the surface facing the electron gun.

(2) The defects form in the alloy independently of its thermal history and they are also observed in pure nickel.

(3) They are not confined to the area irradiated by the electron beam.

(4) The loop diameter ($\sim 80$ Å) is consistent with the formation of each loop from an individual ion impact. An 100 kV oxygen ion produced $10^3$ Frenkel pairs and the maximum loop diameter produced by clustering of the vacancies, if all the interstitials escape to the foil surface, is $\sim 80$ Å.

(5) The loop density after 3 hours' observation in the microscope is $\sim 10^3\ \mu m^{-2}$, which gives a rate of defect production similar to that reported by Pashley and Presland (1961) for gold specimens. Assuming that each loop corresponds to an individual ion impact, the above loop production rate corresponds to an ion irradiation rate of $\sim 10^7\ cm^{-2}\ s^{-1}$, in good agreement with the measurements reported by Howie *et al.* (1966).

It is also possible to differentiate between ion damage of this type and fine precipitates with $P_s \lesssim 0.2$ which also produces black/white lobe contrast. In this particular case, because the ion damage is almost all within layer I, figure 3.27(a), whereas the precipitates are uniformly distributed throughout the foil, $\boldsymbol{g} \cdot \boldsymbol{l}$ has constant sign for loops but varies positive and negative for the precipitates. Figure 4.3(b) shows this effect clearly. Two rows of small TiC particles have been precipitated in the wake of a climbing perfect dislocation, in the manner suggested by Silcock and Denham (1969). The row of particles end at the bottom surface of the foil at A and each particle along the line AX lies at successively higher levels, for example the particles B lie within layer II, figure 3.27(a), and the sign of $\boldsymbol{g} \cdot \boldsymbol{l}$ has changed. Using the rules in section 3.11.1.1, $\boldsymbol{g} \cdot \boldsymbol{l}$ is negative level I and positive level II, figure 3.27(a), and the defects are interstitial. A significant amount of ion damage exhibiting the contrast of vacancy loops is also present in this area, for example D.

### 4.3.2 *Large Black/Black or Black/White Lobe Images*

The size of these images is usually $\sim \xi_g$ and they can arise from precipitates, gas bubbles, dislocation loops, end-on dislocations, stacking fault tetrahedra (table 4.5). The cases of spherically symmetrical strain fields of precipitates or bubbles, together with the images of end-on dislocations, dislocation loops, are well understood. However,

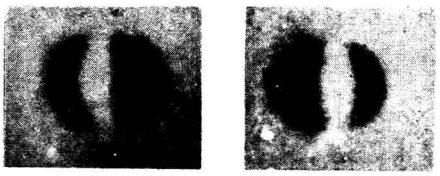

(a) (b)

Figure 4.4 The strain field contrast behaviour of a $\delta'$ $Al_3Li$ precipitate in an aged Al–10.7 at % Li alloy for $\pm \boldsymbol{g}$ [331]

asymmetric strain fields from precipitates or bubbles have only received limited attention so specific conclusions may not be drawn except in a few cases.

The following distinctions may be readily made between the following.

(1) Dislocation loops and precipitates with strain field. The image of the loop will change size on reversing $\boldsymbol{g}$ but that of a precipitate will not. Compare figure 4.4(a),(b) with figure 4.8(d),(e). Note that only precipitates show black/white lobe contrast when near the surface because a loop usually has a smaller strain field, section 3.5.5.1.

(2) Large precipitates with black/black lobes and end-on dislocations because the latter only have black/white lobe images. However, this distinction may be avoided by using thicker regions of the foil where the dislocation end effect is less obvious and they may be detected by tilting the foil 30–40°, that is they are no longer end on. If for some reason very thin regions cannot be avoided, use a number of different $\boldsymbol{g}$ so that the loops or planar precipitate images (which are relatively unaffected by $\boldsymbol{g}$) can be identified. The end-on dislocation images should change significantly under different $\boldsymbol{g}$, for example for a screw dislocation the black/white lobes always on either side of $\boldsymbol{g}$, $\boldsymbol{l}$ perpendicular to $\boldsymbol{g}$, see section 3.4.8.

(3) Precipitates and gas bubbles. The through-focus properties of gas bubbles may be used to characterise these defects, see section 3.13.2.

(4) Large Frank and perfect loops because the former contain stacking fault fringes.

(5) Small Frank loops and perfect loops may be distinguished by obtaining images in $\pm \boldsymbol{g}$ for two {020} reflections such that $\boldsymbol{g} \cdot \boldsymbol{b} = \pm \frac{2}{3}$ for all four $\boldsymbol{b} = \frac{1}{3}\langle 111 \rangle$. Frank loops show reversal of contrast whereas prismatic loops do not, see figure 4.5(a),(b) (Loretto *et al.*, 1966).

(6) The spherical symmetry, or otherwise, of the precipitate strain field may be detected by observing the direction of the line of no contrast for different reflections which should always be perpendicular to $\boldsymbol{g}$. Figure 4.6 shows an example of TiC particles in the nickel-base alloy discussed in section 4.3.1.1. Note that $\boldsymbol{g}$ is not perpendicular to the line of no contrast, that is the strain field

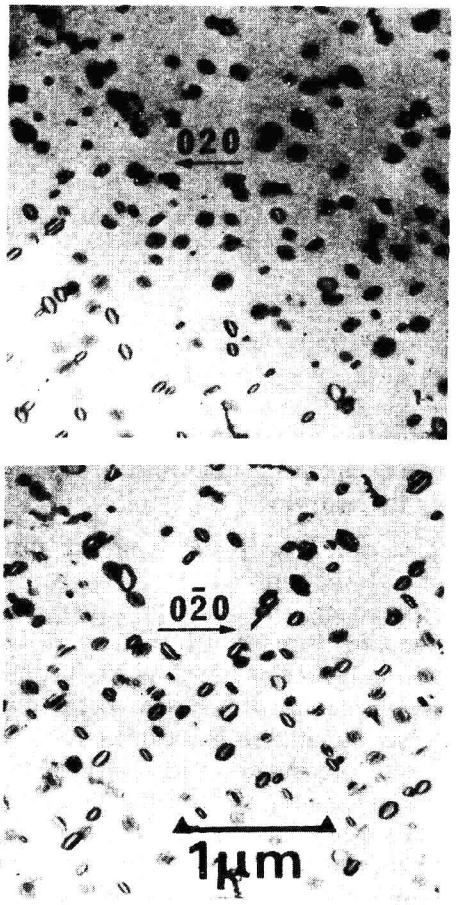


Figure 4.5 BF images of quenched-in dislocation loops in aluminium $\boldsymbol{B}$[001]. The deviation $s$ from the Bragg position is large and the distinction between loops in good and bad contrast is obvious [From Loretto *et al.* (1966), courtesy of *The Philosophical Magazine*]

is asymmetric, and the line of no contrast changes direction depending on $\boldsymbol{g}$.

(7) Note that precipitates may be most easily detected and identified from extra spots in SADP if the volume fraction is high enough. Alternatively they may occasionally protrude from the edge of the foil.

However, the following distinctions are more difficult.

(1) Between black/white precipitate images and particles near the surface and end-on dislocations. This situation is best avoided by using thicker regions and tilting through large angles to reveal the dislocation line.

(2) Any work involving non-spherically symmetrical strain fields.

#### 4.3.2.1 *Identification of coherent precipitates and dislocation loops in a high-phosphorus stainless steel (after B. L. Eyre)*

An example of a contrast analysis including some

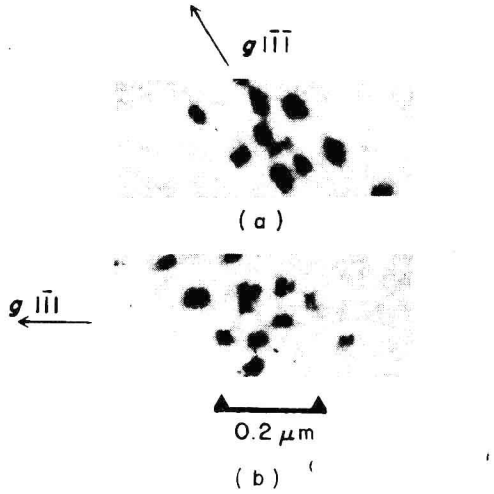


Figure 4.6 BF images of TiC particles in quenched and aged Ni–4.47 wt% Ti–1.96 wt% C observed under different reflections

of the defects discussed in this section is given below for a steel containing 18.18Cr–10.25Ni–0.012C–0.31P–0.60Mn–0.31Si–0.009N in wt% (Rowcliffe and Eyre, 1971). The heat treatments which produce the two defects of interest are given in table 4.6. In the following discussion the importance of metallurgical information, such as annealing behaviour, in addition to contrast behaviour, is clearly demonstrated.

Table 4.6 Heat treatments

| Solution treatment | Ageing treatment | Defect observed |
|---|---|---|
| 1100 °C, $\frac{1}{2}$ hour | 650 °C, 1 hour | type 1 |
| 1100 °C, $\frac{1}{2}$ hour | 500 °C, 1 hour | type 2 |
| 1100 °C, $\frac{1}{2}$ hour | 500 °C, 10 hours | type 2 |

Micrographs were obtained under strong two-beam conditions, see figure 4.7, and the characteristic images of these defects are discussed below.

*Defects 1.* These defects occur in a high density, see figure 4.7(a), and from their black/black lobe contrast could be either precipitates with strain fields, gas bubbles or dislocation loops. However, their contrast behaviour under different reflections enables some of these to be rejected, for example the following possibilities.

(1) The line of no contrast is always approximately perpendicular to $\boldsymbol{g}$, compare figure 4.7(a)–(c).

(2) Large black/white lobes are observed when the defects are near the surface, figure 4.7(a) at A, but there are no black/white depth oscillations.

(3) The size of most of the images is $\sim \xi_g$.

The above behaviour is typical of Ashby–Brown contrast from precipitates with an approximately